

Rocket Observations of Far-Ultraviolet Dust Scattering in NGC 2023

Eric B. Burgh¹, Stephan R. McCandliss, Paul D. Feldman

Department of Physics and Astronomy, The Johns Hopkins University, Baltimore, MD 21218

ABSTRACT

The reflection nebula NGC 2023 was observed by a rocket-borne long-slit imaging spectrograph in the 900 – 1400 Å bandpass on 2000 February 11. A spectrum of the star, as well as that of the nebular scattered light, was recorded. Through the use of a Monte Carlo modeling process, the scattering properties of the dust were derived. The albedo is low, 0.2 – 0.4, and decreasing toward shorter wavelengths, while the phase function asymmetry parameter is consistent with highly forward-scattering grains, $g \sim 0.85$. The decrease in albedo, while the optical depth increases to shorter wavelengths, implies that the far-UV rise in the extinction curve is due to an increase in absorption efficiency.

Subject headings: ultraviolet: ISM – ISM: dust, extinction – reflection nebulae – ISM: individual (NGC 2023)

1. Introduction

The far-ultraviolet absorption and scattering properties of interstellar dust are not well determined, yet they are responsible for the regulation of the penetration of far-UV light into interstellar clouds. This energetic radiation can ionize atomic species and photodissociate molecules, and thus plays an important role in the ionization, chemical, and thermal balances of the interstellar medium. The extinction curve along lines of sight through the ISM is a measure of the combined effects of absorption and scattering by dust, and several studies indicate a relationship between the morphology of the far-UV extinction curve and diagnostics of the conditions within interstellar clouds (Joseph, Snow, & Seab 1989; Jenniskens, Ehrenfreund, & Désert 1992; Burgh et al. 2000).

However, it is important to note that the actual attenuation of radiation in a cloud depends strongly on the far-UV scattering properties of the grains responsible for the extinction, even when the extinction rises sharply in the far-UV (Flannery, Roberge, & Rybicki 1980). This is especially true for forward scattering grains. These will re-

move photons from line of sight observations toward stars, producing extinction, but may not appreciably affect the radiation field within clouds, as the photons will be only slightly deflected from their original direction. Thus, it is necessary to understand the breakdown of the extinction curve into absorption and scattering efficiencies separately, as well as the detailed properties of the dust itself, such as the albedo and the degree of forward scattering.

Reflection nebulae provide useful sites for studying the scattering properties of interstellar dust grains. In many cases the illumination is due to a single star and the geometrical distribution of the dust can be constrained, or at least closely approximated. As the illuminating source is contained very close to or within the nebula, its spectrum can often be measured simultaneously with the nebular scattered light by the same instrument. This allows for the direct comparison of the source to the scattered light independent of the instrument calibration. The dust scattering properties may then be derived through a comparison of the observations to an appropriate model.

A few bright nebulae have been studied in the ultraviolet, including the Merope nebula (Andriesse, Piersma, & Witt 1977; Witt 1985), NGC 7023 (Witt et al. 1982, 1992, 1993; Murthy

¹Current Address: Space Astronomy Laboratory, University of Wisconsin at Madison, 1150 University Avenue, Madison, WI 53706

et al. 1993), the Scorpius OB association (Gordon et al. 1994), and IC 435 (Calzetti et al. 1995). This work reports on the observations of the reflection nebula NGC 2023 with a far-UV (900–1400 Å), rocket-borne long-slit imaging spectrographic telescope.

NGC 2023 is a bright reflection nebula located $\sim 23'$ SE of ζ Ori. The illuminating star HD 37903 is of B1.5V spectral type and is embedded in the L1630 molecular cloud at a distance of 450–500 pc (de Boer 1983). It is one of the brightest reflection nebulae in the sky and well-studied at many wavelengths including [C II] 158 μm (Howe et al. 1991; Jaffe et al. 1994), carbon recombination lines (Knapp et al. 1975; Wyrowski et al. 2000), far-infrared dust emission (Harvey, Thronson, & Gatley 1980; Mookerjee et al. 2000), and infrared H_2 emission (Gatley et al. 1987; Field et al. 1998; McCartney et al. 1999; Martini, Sellgren, & DePoy 1999).

A photometric study of the nebular surface brightness was performed by Witt, Schild, & Kraiman (1984, WSK hereafter) at visible wavelengths. In their work, a radiative transfer model that incorporated multiple scattering was used to derive the dust scattering properties from photometric observations of the nebular surface brightness profiles in the *uvby* and *BVRI* bandpasses ranging from 3500 and 10000 Å. In this work, this method is extended to far-ultraviolet wavelengths; because the optical depths increase to shorter wavelengths, it is very important to use a similar detailed radiative transfer model that accounts for multiple scattering.

2. Instrument and Observations

2.1. Instrument

The telescope flown was a modified version of the Faint Object Telescope (FOT) developed by the Johns Hopkins Sounding Rocket Group (Hartig et al. 1980). The FOT comprises a 40 cm diameter, f/15.5 Dall-Kirkham telescope with a long-slit imaging spectrograph. To maximize the efficiency in the far-UV bandpass, the optics were overcoated with ion beam deposited SiC (Keski-Kuha et al. 1988). At the focus of the telescope is a mirror, which acts as the field stop for a slitjaw viewing camera and has cut into it a long, narrow (200" x 12") slit, defining the entrance aperture to

the spectrograph.

The spectrograph employs a 400 mm diameter Rowland Circle mounting with $\alpha = 8^\circ 6'$ and $\beta = 0^\circ$ (McCandliss et al. 1994). It contains a holographically-ruled, astigmatism-corrected diffraction grating used in -1 order. The spectrograph is sealed with a motorized gatevalve, which operates during flight. The detector is a Z-stack of microchannel plates with a KBr photocathode and a delay-line anode for readout (Siegmond et al. 1993). Additionally, an onboard calibration lamp (McCandliss et al. 2000) was flown to provide an in-flight wavelength calibration.

2.2. Observations

The sounding rocket experiment was launched aboard a Black Brant IX sounding rocket from White Sands Missile Range, New Mexico (106°3' W, 32°4' N) on 2000 February 11, at 20:27 MST. The entire flight time was approximately 15 minutes, with 400 seconds (from T+100 to T+500) spent with the detector high voltage on. NGC 2023 was acquired at T+175 and pointing stability was established through the use of a wide field-of-view ($\pm 1^\circ$) startracker, which maintained “lock” on ζ Ori during the observations.

The central star of NGC 2023, HD 37903, was observed for 125 seconds. However, the pointing was stable for only 98.5 seconds, with the star well situated in the slit and a steady count rate. Only these data are considered here and are called the “on-star” pointing. A far-UV spectrum of the star was recorded, as well as the nebular scattered light to a distance of $\pm 60''$ along the slit, which was oriented in the north-south direction. The remainder of the flight was divided into three offset pointings to explore the scattered light distribution and to search for fluorescent emission from molecular hydrogen (H_2).

3. Data

The data from the rocket experiment were telemetered to the ground in the form of a bit stream. For every detected photon, as well as calibration lamp photons, dark counts, and possible detector hot spots, X , Y , and T information was encoded in the stream. X and Y correspond to the position on the detector of the event and T the time of the event during flight. These data

may be binned spatially and/or temporally.

A spectral image was created, shown in Figure 1, by compressing the entire flight’s data into an X - Y image. The image has been corrected for several detector effects, as well as for spacecraft jitter during the “on-star” portion. Present in the image are the continuum flux from HD 37903 (the horizontal stripe) and the nebular scatter surrounding it. The strong vertical line at 1216 Å is the H I Ly- α airglow emission. Airglow lines at 1026 Å and 1304 Å are also present. At the top of the image is a spectrum of atomic, ionic, and molecular nitrogen provided by the onboard calibration lamp. As the light from the lamp did not enter the spectrograph through the entrance slit, there is a slight zero-point offset in the dispersion direction.

The calibrated stellar flux, computed from the central 10 pixels of the detector, is shown in Figure 2. The flux is consistent with measurements made of the star by the Hopkins Ultraviolet Telescope (HUT) (Buss et al. 1994). Clearly seen in the spectrum are several interstellar and stellar absorption features, including those of H I, C II, C III, O I, Si II, and the H₂ Lyman and Werner bands. Also, the strong effect of dust extinction is apparent, since the intrinsic spectral energy distribution of a B1.5V star rises to shorter wavelengths. The feature marked “grid” is an instrumental artifact due to the vignetting of light by the QE enhancement grid on the detector.

Due to the two-dimensional nature of the long-slit imaging spectrograph, a spatial profile of the nebular scattered light can also be extracted from the data. The data were compressed in the spectral dimension, excluding the region around Ly- α , binned up spatially along the slit as a surface brightness, assuming that the scattered light fills the slit, and referenced to the flux of the star. This produced a slit profile of the ratio of the nebular surface brightness to stellar flux (S/F_*) (see Figure 3), which is independent of the absolute detection efficiency of the spectrograph. Overplotted is the instrumental line spread function (LSF) as determined from laboratory measurements using a windowless vacuum ultraviolet collimator (Burgh et al. 2001). The inner region is dominated by light from the star, but outside of $\pm 10''$ there is negligible contribution from the LSF and the nebular flux can clearly be observed, falling off exponentially with distance from the central star. To

the south of the central star, a dust lane appears to intersect the nebulosity, causing a depression in the flux centered at $\sim 50''$ south.

4. Extinction Curve and R_V

The derivation of dust scattering properties in reflection nebulae is strongly model dependent. Relevant parameters include the physical depth of embedment of the illuminating star in the dust cloud and the wavelength dependence of the dust opacity. A depth of 1 pc was assumed by WSK. This is consistent with the size of the nebula as determined from the emission measure of carbon recombination lines (Knapp et al. 1975). At the distance of the L1630 cloud, this corresponds to $\sim 450''$. The wavelength dependence of the dust optical depth is derived from the extinction curve; however, it is very important to determine what fraction of the extinction along the line of sight to the illuminating star is associated with the nebula itself and what fraction is due to foreground material. The optical extinction through the L1630 cloud is estimated at $A_V \sim 40$ mag (Harvey, Thronson, & Gatley 1980); because the visible extinction toward HD 37903 is $A_V \sim 1.4$ mag, it is clear that the star is located on the near side of this dense cloud. From far-infrared (FIR) measurements, Harvey, Thronson, & Gatley (1980) suggest that the extinction from FIR-emitting dust should account for a significant fraction of the total extinction. Since this dust emission is due to the processing of UV photons, it is likely that most of the extinction along the line of sight is associated with NGC 2023.

To determine the extinction curve, the “pair method” was used, in which the spectrum of an unreddened star of the same spectral type is compared to that of HD 37903. Following de Boer (1983), HD 37744 was used as the comparison star for HD 37903. This star, only $\sim 37'$ away from HD 37903, lies to the west of the L1630 cloud and exhibits only a mild amount of reddening ($E_{B-V} = 0.05$) (Hardie, Heiser, & Tolbert 1964; Crawford et al. 1971). Its spectroscopic parallax suggests that it lies only ~ 50 pc more distant than HD 37903 (de Boer 1983), and as such samples essentially the same foreground extinction. The difference in reddening is thus due to the dust in the L1630 cloud that lies between the front surface

of the cloud and the embedded star, and the extinction curve derived from comparing these two stars should be indicative of the extinction properties intrinsic to the nebular dust, canceling out the effects of the foreground dust along the Orion line of sight.

Low-dispersion data of both HD 37903 and HD 37744 were obtained from the *International Ultraviolet Explorer (IUE)* archive. For each star, the short- and the long-wavelength data were joined to a common wavelength grid ranging from 1150 to 3350 Å. The extinction curve, shown in Figure 4, was derived from the ratio of the stellar fluxes, normalized to the difference in E_{B-V} , and fitted with the parameterization of Fitzpatrick & Massa (1990). The extinction curve, $k(x) \equiv E_{\lambda-V}/E_{B-V}$ with $x = \lambda^{-1}$, is converted to optical depth through the use of the ratio of total-to-selective extinction, $R_V [\equiv A_V/E_{B-V}]$, following $\tau = (k(x) + R_V)E_{B-V}/1.086$.

The value for R_V was reassessed for this work. The extrapolation of the extinction curve to infinite wavelength, or zero frequency, at which absolute extinction (A_λ) would be zero, provides for the calculation of R_V . The value of R_V thus determined depends strongly on the functional form of the extinction toward zero frequency. It is useful to have extinction data at low frequency and near-infrared (NIR) photometric observations are typically used.

It has been found that the shape of the NIR extinction curve is very uniform along almost all lines of sight (Rieke & Lebofsky 1985; Whittet 1988; Cardelli, Clayton, & Mathis 1989; Martin and Whittet 1990), taking the form of a power law ($A_\lambda \propto \lambda^{-\alpha}$) between $\sim 1 \mu\text{m}$ and $5 \mu\text{m}$. At longer wavelengths, emission from dust can contaminate photometric observations and complicate the determination of extinction. Martin and Whittet (1990) expand this power law in terms of the extinction curve and R_V in the following form:

$$\frac{E_{\lambda-V}}{E_{B-V}} = e\lambda^{-\alpha} - R_V. \quad (1)$$

For HD 37903, the NIR photometric data from the literature, listed in Table 1, were averaged together and the colors $\lambda-V$ determined. The photometry for V and $B-V$ are taken from Hardie, Heiser, & Tolbert (1964) ($V=7.84$, $B-V=0.10$), Lee (1968) ($V=7.83$, $B-V=0.11$), and Racine

(1968) ($V=7.82$, $B-V=0.09$). These were averaged together to produce a V magnitude and $B-V$ color. By comparing the NIR colors to the intrinsic colors for a B1.5V star (Koornneef 1983), the color excesses $E_{\lambda-V}$ were computed. These were then normalized by E_{B-V} and a least squares fit was performed with the Martin and Whittet (1990) power law described above (see Figure 5). This method produced a determination of $\alpha = 1.8 \pm 0.9$ and $R_V = 3.83 \pm 0.40$. The large error in these values is mainly due to the uncertainty in the L and M band photometry.

These results compare well with previous determinations of α and R_V . Whittet (1988), from an analysis of an extensive data set obtained from the available literature at the time, found an $\alpha = 1.70 \pm .08$. Cardelli, Clayton, & Mathis (1989) used the Rieke & Lebofsky (1985) curve, which has an $\alpha \simeq 1.6$ and Landini et al. (1984), through observations of the hydrogen recombination lines in H II regions, found values for α and R_V of 1.85 ± 0.05 and 4.11 respectively. R_V can also be computed from color excesses following $R_V = 1.1E_{V-K}/E_{B-V}$, from the standard van der Hulst theoretical curve, and gives a value of $R_V = 3.7$. These are comparable to the value of R_V based on the above calculation within the error introduced by the uncertainty in the NIR photometric measurements.

5. Monte Carlo Model Fitting

An analytic solution for the surface brightness of a reflection nebula can be computed in the case of single scattering. However, this would only be accurate for optically thin nebulae. Roark et al. (1974) have shown, through the use of Monte Carlo methods, that multiple scattering can have a significant effect on the observed surface brightness distribution. The intrinsic random nature and statistical approach to the scattering process has allowed for radiative transfer models of dusty nebulae to be constructed, including some with arbitrary dust density and source distributions (Witt 1977; Yusef-Zadeh, Morris, & White 1984; Wood and Reynolds 1999; Gordon et al. 2001).

To determine the dust scattering properties in NGC 2023, a Monte Carlo dust radiative transfer model was developed following the algorithm described in full detail by Gordon et al. (2001). To

simplify the modeling process and reduce the computational demands, the nebula was modeled as a single star embedded in a spherical dust cloud of constant density and finite extent.

Using this Monte Carlo process, a model nebula can be created for a given radial optical depth, angular size of the nebula, and the dust’s albedo, a , and phase function asymmetry parameter, g , assuming the phase function of Henyey & Greenstein (1941). The first two are set and the dust properties a and g are varied until agreement with the observations are maximized. The following section discusses the results of fitting models to the data and the resultant derivation of the dust scattering properties.

5.1. Radial Profile Fitting

The data were binned spatially to produce a slit profile, compressing the entire wavelength range into a one-dimensional profile, excluding a 10 Å band (one slit width) around the Ly- α geocoronal airglow line at 1216 Å. The error for each bin was computed using Poisson statistics, i.e. $\sigma_{\text{bin}} = \sqrt{N}$, with N the number of counts in the spatial bin. The inner $\pm 5''.5$ of the profile is dominated by the star and we take the total counts in this region to correspond to the stellar flux (F_*).

The flat-field corrected ratio of the nebular surface brightness to stellar flux, S/F_* , for the “on-star” exposure is shown with logarithmic scaling in Figure 3. Positive offsets are to the north. Outside of the inner region, where the instrumental LSF causes the stellar flux to dominate, the nebular brightness falls off exponentially by about an order of magnitude. Only the region inside of $\pm 60''$ contained data with a count rate above the dark rate. To the south, a dust lane cuts in front of the nebulosity at around $-50''$.

A grid of models for various values of a and g corresponding to the far-UV optical depth was generated. The optical depth used was a stellar flux intensity weighted average of the $\tau(\lambda)$ derived from the extinction curve in Section 4. For each model in the grid, the χ^2 statistic was computed by comparing the model to the data following

$$\chi^2 = \sum_i \left(\frac{y_i - y(x_i; \tau, a, g)}{\sigma_i} \right)^2. \quad (2)$$

In this definition, y_i and σ_i are the data and their

respective errors for the i th spatial bin. The term $y(x_i; \tau, a, g)$ is the model prediction for S/F_* as a function of radius for the given optical depth and the input values for a and g . The sum is over the region $r = 10 - 60''$ on both the north and the south sides of the central star. The instrumental LSF was added in to the model fits; however, its presence had no effect on the fitted parameters as the contribution from the star due to the LSF is negligible outside of $10''$. The best fit parameters were determined from the model that gave the minimum value of χ^2 . The best fit parameters for the full experiment bandpass are listed at the top of Table 2 and the model is shown overplotted on the data in Figure 6. Additionally, as the profile showed some asymmetry, the north and south sides of the star were fitted separately. These produced different fit results; however, that may be more likely due to a variation in the dust distribution than actual differences in the scattering characteristics.

To obtain the wavelength dependence of the dust scattering properties, the data were divided into several wavelength regions. Six wavelength regions were chosen across the full bandpass, and the above procedure was used to fit these data, with a few exceptions. The spatial range was limited to less than $60''$. This is due to the fact that as fewer data were used the contrast between the nebular scattered light and the background was worse and the outer limit of the range was decreased to avoid fitting the background. The maximum fitting radius was chosen for each bandpass so that the signal-to-noise ratio (S/N) of the spatial bins was always greater than one. The widths of the bandpasses were chosen so that this radius was greater than $30''$. The wavelength ranges and maximum radii are listed in Table 2. For the shorter wavelength bandpasses, in which there are considerably less data due to the line-of-sight extinction, a coarser spatial binning was used. This provides more counts per spatial bin, which results in a higher S/N per bin, and thus a larger radius before the S/N dropped to one. If the maximum radius were too close to the star, the small number of data points would limit the constraint on g . The best fit dust parameters are listed in Table 2.

Confidence intervals were based on the χ^2 contours. Figure 7 shows the χ^2 contours for the 1240–1295 Å bandpass. The χ^2 fitting produces

asymmetric error bars, with most of the confidence tending toward lower g and higher a . Thus, it is apparent that there is a strong coupling between a and g . Any random or systematic effects that would change the value of g could have a corresponding change in a .

The derived dust parameters from Table 2 are plotted in Figure 8. For comparison, the predicted values from Weingartner & Draine (2001) for values of R_V of 3.1, 4.0, and 5.5 are overplotted. We find g increases mildly across the bandpass, while a falls toward shorter wavelengths.

5.2. Spectral Fitting

To achieve a better S/N , the data can be binned up spatially and the ratio of the nebular surface brightness to stellar flux shown as a function of wavelength rather than slit position. However, this removes the ability to fit g in an independent manner, so for this procedure a constant value of g was assumed, as supported by the results of the previous section. Then, as a function of wavelength, the S/F_* can be used to derive the albedo directly through the model fitting.

The data are binned in the spectral dimension, compressing the spatial range from $10 - 60''$ into one bin for each wavelength range. Because the nebular scattered light is a diffuse source and is expected to fill the slit, the data were binned by one slit width, or 10 \AA across the full wavelength region, excluding the Ly- α region, to 1030 \AA . At shorter wavelengths, the detected count rate for the nebular scattered light is consistent with the background. The stellar spectrum was also smoothed by one slit width before the ratio was determined. The derived S/F_* is shown in Figure 9. It is virtually constant at all wavelengths, despite a rising optical depth toward shorter wavelengths.

The data are compared to a grid of models with different albedos for an assumed value of $g = 0.85$ across the bandpass. Since the g from the radial profile fitting was fairly constant, the average value is used in the fitting here. The best fit albedos are shown in Figure 10. There is a decrease in albedo as the wavelength decreases. This is consistent with the results derived from the profile fitting above (see Figure 8). Overplotted are the predictions from Weingartner & Draine (2001) for

a few values of R_V . The derived albedos agree very well with the predictions.

The relative efficiencies for both scattering and absorption, Q_{scatt} and Q_{abs} , can be derived from the albedo, since $a = Q_{\text{scatt}}/Q_{\text{ext}}$. Therefore, $Q_{\text{scatt}} = aQ_{\text{ext}}$ and $Q_{\text{abs}} = (1 - a)Q_{\text{ext}}$. The extinction efficiency, $Q_{\text{ext}} (= Q_{\text{abs}} + Q_{\text{scatt}})$, is proportional to the extinction curve, and thus to τ . The derived relative efficiencies are shown in Figure 11, along with the extinction curve, in units of A_V/E_{B-V} . It is apparent that the rise in the far-UV extinction curve of NGC 2023 is due to an increase in absorption, whereas the scattering efficiency is nearly constant.

5.3. Systematics

As mentioned earlier, the derivation of the dust parameters a and g is sensitive to the modeling process. There are several sources of systematic error that can affect the best fit parameters. This section discusses some of these sources and describes the effects they have on the derived dust properties.

In the data preparation process, it was assumed that all of the detected photons within $\pm 5''$ of the peak of the radial profile are stellar in origin. However, a contribution from scattered light at small angles, which would be included with the stellar light, would result in an underestimation of S/F_* and hence the derived albedo. This effect would become increasingly important as all the parameters, τ , a , and g , increase. As the optical depth increases, the contrast between the escaping stellar light, F_* , and the nebular scattered light would decrease due to the increased probability of interaction. An increase in albedo would make the nebular scattered light brighter, and higher values of g increase the chance of scattering into the line of sight at small angles from the star.

Assuming that the constant density of the model can be continued to the position of the star, the Monte Carlo model was used to estimate the number of nebular photons near the center that would be mixed in with the stellar light. For $\tau = 2 - 3$, $a = 0.2 - 0.4$, and $g = 0.8 - 0.9$, the fraction of nebular contribution to the stellar flux ranges from 5 - 20%. However, based on C II emission, Knapp et al. (1975) conclude that there may be a dust-free H II region surrounding

HD 37903 with a radius as large as $\sim 25''$, and Harvey, Thronson, & Gatley (1980) suggest that the inner 0.04 pc ($18''$) is clear of dust. A “hole” in the dust distribution would reduce the contribution from scattered light in the vicinity of the star, and the modeled contamination is thus an upper limit. Decreasing the stellar flux in the model fits as described above resulted in an increase in the fitted albedo by an amount proportional to the flux reduction, but did not affect g ; i.e., a decrease in flux by 10% corresponded to an increase in the derived value of a by 10%.

A spherical geometry was assumed in the modeling process. For the L1630 cloud, a plane-parallel slab model may be more appropriate. However, if the depth of embedment, and thus the radius of the sphere in the model, is large relative to the extent being observed as projected onto the sky, the difference between the sphere and slab models is negligible. We used the value from WSK of 1 pc for the radius, and therefore the model fits were performed on the inner 0.5–1.0' of an assumed $\sim 7'$ nebula. If the depth of embedment, and hence the radius of the spherical model, is of lower value, then the fitted g values decrease. Also, the correlation of a and g , as apparent from the χ^2 confidence intervals shown in Figure 7, is weaker for smaller depth.

At too small a radius relative to the observed extent, the assumption of spherical symmetry is no longer sufficient to describe the geometry. In this case, it is possible that the observed nebular surface brightness distribution can be explained by a slab geometry of shallow depth but large horizontal extent. There do exist degeneracies between the two geometries, such that a spherical cloud of given a and g can appear identical to a slab with the star embedded less deep and lower values of g but observed out to radii larger than the actual depth of embedment. The value of 1 pc for the radius produces fits to the visible wavelength surface brightness with reasonable values for a and g (WSK).

The optical depth used in the modeling is dependent on the far-UV extinction curve. The primary systematic error affecting τ_{UV} is from the propagation of the L and M band photometric errors in the determination of R_V . Although these were large, the resultant uncertainty in R_V does not have a large effect on the optical depth in the

UV and the fitted parameters are modified only slightly ($\lesssim 10\%$). If less of the extinction were associated with the nebula itself, the albedo would increase; however, not more than half can be foreground or the far-UV albedo would be driven to the maximum value of 1.0. There is also an implicit assumption that, for the lack of a far-UV spectrum of HD 37744, the UV extinction curve as derived from *IUE* can be extrapolated to shorter wavelengths than 1150 Å following the parameterization of Fitzpatrick & Massa (1990).

As already mentioned, a constant dust density distribution was assumed in the modeling process. This greatly reduced the computation time, because the distance each photon traveled was simply linearly proportional to the optical depth along all directions through the model dust cloud. WSK, on the other hand, assumed a weak radial falloff in the density distribution. Such a radial density dependence could account for some of the observed falloff in nebular surface brightness and reduce the value of g necessary to fit the slit profiles. Although there is the possibility of large scale density variations, the nebula appears to be fairly smooth in both the blue, as observed by the digitized sky survey, and the far-UV, as shown in the slit profile in Figure 3.

It should be noted that the predicted dust properties, such as those of Weingartner & Draine (2001), to which the results have been compared, are based on Mie scattering theory, which solves for the exact electromagnetic fields in a spherical or cylindrical dust grain. However, it is clear from polarization studies that dust grains in the interstellar medium are not spherical. The more probable situation is that dust grains collide and either stick together or shatter, producing grains of a more random distribution of shapes (Mathis & Whiffen 1989; Bazell & Dwek 1990; Fogel & Leung 1998, e.g.). Savage & Mathis (1979) point out that the Henyey-Greenstein phase function is an analytic function that approximates the results from Mie theory and may not represent the true scattering phase function.

Witt et al. (1993) have pointed out that dust scattering is often accompanied by fluorescent emission of H_2 . It is therefore necessary to account for any contribution from the H_2 far-UV fluorescent cascade to the dust scattered continuum. Fluorescently excited H_2 is indeed present

as evidenced indirectly by the detection of absorption lines from highly excited vibrational states (Meyer et al. 2001). More direct evidence is offered by the *IUE* spectrum, SWP 38082, which exhibits the same characteristic pair of fluorescent H_2 emission lines at 1577 and 1608 Å as seen in the IC 63 (SWP 33898) spectrum where H_2 fluorescence has been confirmed (Witt et al. 1989). The scattered continuum in NGC 2023 has an $S/F_* \sim 10^{5.6}$ in the wavelength region longward of 1700 Å, and the H_2 emission peaks at ~ 3 times this value.

However, the *IUE* spectrum of NGC 2023 was acquired at a position $\sim 75''$ east-north-east of HD 37903, coincident with a bright infrared emitting knot as revealed in high spatial resolution images of the nebula. These images, which isolate specific vibrational quadrupolar transitions in the ground electronic state of H_2 , generally show a clumpy distribution (Field et al. 1998; Takami et al. 2000). In particular, the Takami et al. (2000) images shows the region to the north of HD 37903 to be devoid of H_2 infrared emission within the extent of the rocket experiment’s slit. To the south there are two lanes; one is rather close, $\sim 10 - 20''$, to the central star and comparable in brightness to the east-north-east knot, and the other (the southern bar) is $\sim 70''$ south of HD 37903 and brighter, with a void of emission in between. Martini, Sellgren, & DePoy (1999) have observed the infrared emission spectroscopically in the region to the south of the star that is spatially coincident with our slit. They find that the brightest infrared H_2 emission lies in a bar between $67''$ and $84''$ south that is ~ 3.5 times stronger than the region closer to the star. They also show that the infrared continuum emission is essentially negligible in the southern bar and increases towards the star, becoming comparable to the H_2 emission close in.

The southern bar of the nebula was observed within our slit; however, the data here are consistent with the background, with a 2σ upper limit of $S/F_* = 10^{5.5}$. As this is the brightest region of H_2 infrared emission along the slit, we conclude that the region closer to the star, in which we detect $S/F_* = 10^{6.5} - 10^7$, has a negligible contribution from far-UV H_2 fluorescent emission. The asymmetry between the profiles in the north and the south sides of the star mentioned previously is thus

more likely due to asymmetries in the dust distribution than additional emission from H_2 . This asymmetry has only a small effect on the fitting of the modeled slit profile to the data.

We note that the rocket flight included two off-set pointings in the north-eastern portion of the nebula, $\sim 45''$ from the star, which do show an excess of emission from the best-fit scattered light model by a factor of $\sim 2 - 4$. Although the spectral resolution of the sounding rocket is ideal for investigating dust scattered light it is insufficient for unambiguously detecting suspected far-UV fluorescent emissions from H_2 .

6. Discussion and Conclusions

The results described above show that the dust in the reflection nebula NGC 2023 is highly forward scattering and has a low albedo that decreases with decreasing wavelength. These results are in good agreement with the predictions of a and g based on the fitting of extinction curves (Li & Draine 2001; Weingartner & Draine 2001). The rise in the far-UV extinction curve is due to an increase in the absorption efficiency of the dust grains, whereas the scattering efficiency appears constant. This suggests that the scattering is being performed by large grains, while a low-albedo small grain population may be the cause of the short wavelength absorption.

The approach taken here is very similar to that of previous work on other reflection nebulae. NGC 7023, for example, is a similar, but more extincted, nebula to NGC 2023. It has been observed extensively in the ultraviolet, by *IUE* (Witt et al. 1982), the Ultraviolet Imaging Telescope (UIT) (Witt et al. 1992) and the Hopkins Ultraviolet Telescope (HUT) (Murthy et al. 1993) as part of the Astro-1 mission, and *Voyager 2* (Witt et al. 1993).

The initial study of NGC 7023 with *IUE* suggested more isotropic scattering in the UV than the visible, but the measurements with UIT provided more detailed surface brightness profiles and Witt et al. (1992) conclude that the dust in that nebula is forward scattering ($g \sim 0.70$). The UIT measurements indicated a high albedo ($a \sim 0.6$), similar to that in the visible, but the short wavelength limit was 1400 Å. The HUT measurements extended into the windowless ultraviolet.

let bandpass covered by the sounding rocket experiment. Murthy et al. (1993), using a similar Monte Carlo method, also found that the albedo was high ($\sim 0.6 - 0.7$) in the 1000–1400 Å range, but decreasing to shorter wavelengths. They note that their derived albedo would decrease if more of the dust can be associated with the nebula. Witt et al. (1993) show models for three different optical depth radii in their fitting of the *Voyager* data, resulting in dust albedos at $\lambda = 1000$ Å of $0.45 - 0.26$, with each case showing a clear decline (about 25%) when going from 1400 to 1000 Å.

Calzetti et al. (1995) observed the reflection nebula IC 435, which is very near NGC 2023 in Orion. Their data were taken with *IUE* and were intended to investigate the scattering properties near the 2200 Å bump. Also employing a Monte Carlo model, they derived the dust albedo and phase function asymmetry parameter. The results indicate a drop in albedo at the bump, but rising albedo toward the short wavelength limit of their observations.

It might be expected that, because this nebula appears to also be in the L1630 cloud, the dust characteristics would be similar to those of NGC 2023. However, HD 38087, the central star of IC 435, appears to have a lower than average far-UV rise, and Cardelli, Clayton, & Mathis (1989) find an R_V of 5.3. Aiello et al. (1988) list a value of $R_V = 4.86$ for HD 38087, but it is clear that the extinction toward this nebula is more consistent with a dense region where the dust grains may be larger than average. Also, as this star is of spectral type B5V, the dust environment around the star may be different than that of NGC 2023 if any processing of the dust grains occurs due to the high ultraviolet flux of the hotter HD 37903. However, Calzetti et al. associate only $\sim 20\%$ of the extinction along the line of sight to the nebula itself. This would indicate that the foreground material, which would therefore account for most of the extinction curve, has the dust properties of a dense environment. This is inconsistent with the calculation of the extinction curve toward HD 37903 as described in Section 4, which indicates little foreground extinction toward the L1630 cloud. Had they used a higher optical depth in their Monte Carlo model, their derived albedos would be of lower value, more in agreement with the results derived here.

Measurements of dust scattering properties through observations of the diffuse galactic light (DGL) have significant scatter. Some recent ultraviolet measurements have been made. Observations with the Berkeley UVX spectrometer (Hurwitz, Bowyer, & Martin 1991) indicate a low a , but also a low g in the 1400–1850 Å bandpass. Witt, Friedmann, & Sasseen (1997) found, with the Far Ultraviolet Space Telescope (FAUST) on board the Atlas-1 mission, an albedo of 0.45 and $g = 0.68$ in the same bandpass. Schiminovich, Friedman, Martin, & Morrissey (2001) obtained similar results from modeling the observations from a wide-field ultraviolet sounding rocket experiment, finding $a = 0.45 \pm 0.05$ and $g = 0.77 \pm 0.1$ at 1740 Å. These slightly lower albedos for the diffuse ISM, relative to those found in the denser regions of NGC 7023 and IC 435, have been associated with a dust size distribution including more small grains than average.

There is a large spatial variability to Galactic interstellar extinction, particularly in the ultraviolet. Witt et al. (1993) point out that if these variations are due to changes in the contribution of various grain components to the total extinction then it may be expected that nebula in differing environments may show different far-UV dust albedos.

Though agreeing with the predictions of Weingartner & Draine (2001), the albedo of the dust in NGC 2023 appears to be more consistent with the observations of lower albedo dust in the diffuse ISM as determined from measurements of the DGL, even though it resides within a reflection nebula with an R_V indicating a denser than average environment. Some of this discrepancy could be due to the assumption that the dust in the nebula is homogeneous. Witt & Gordon (1996) have performed simulations of the radiative transfer through two-phase clumpy dust of various filling fractions. Their models suggest that radiative transfer techniques based on homogeneous models can underestimate the albedo when applied to inhomogeneous nebulae. This effect becomes more significant at higher values of g and τ . In their study of the infrared scattering properties in NGC 2023, Sellgren, Werner, & Dinerstein (1992) suggest that the dust may be clumpy in order to reconcile the J , H , and K band surface brightness measurements with the UV and visible measure-

ments.

It is critical to determine the far-UV scattering properties of dust in order to understand the depth dependent effects of the penetration of far-UV photons into interstellar clouds. In their study of the photodissociation of carbon-bearing molecules, van Dishoeck & Black (1989, vDB hereafter) show that varying the morphology of the extinction curve can cause order of magnitude changes in the central photorates in translucent clouds, in particular for CN and CO, which photodissociate at wavelengths shorter than 1100 Å. These effects may have been observed in the studies of Joseph, Snow, & Seab (1989) and Burgh et al. (2000). However, it should be noted that the vDB study assumed the dust scattering characteristics of Model 2 of Roberge, Dalgarno, & Flannery (1981), which has an $a = 0.6$ and $g = 0.5$. These values are not consistent with the results found here, nor with many of the other studies, nearly all of which find a higher value of g in the ultraviolet. Had vDB used the dust properties indicated in this study of NGC 2023, their photorates may have been different. The lower albedos indicated here would drop the dissociation rates due to the stronger attenuation by the dust; however, the more forward-scattering grains could possibly counteract that effect by increasing the probability that a photon might get deeper into the cloud before interacting with either a dust grain or molecule.

Although it is very important to determine the ultraviolet scattering properties of dust, it is clear that there are several inherent difficulties in the modeling of scattered light in reflection nebulae. The most important being the geometry and distribution of the dust relative to the illuminating source. Further studies of the far-infrared emission from dust, in conjunction with these and other far-ultraviolet measurements of dust scattered light, may help to constrain the geometry and thus limit the introduction of systematic errors into the determination of the dust scattering properties.

The authors would like to extend their gratitude to Russell Pelton for the vital role he plays in the continuing success of the JHU Sounding Rocket Group. We would like to acknowledge NASA's Wallops Flight Facility and the NSROC contractor, as well as the support personnel at the

White Sands Missile Range and the Physical Sciences Laboratory of NMSU. We would also like to thank Brad Frey and Geoff Brumfiel for technical assistance. Additionally, we are thankful for useful discussions with Daniela Calzetti and Richard Henry. This work was supported by NASA grant NAG5-5122 to The Johns Hopkins University.

REFERENCES

- Aiello, S., Barsella, B., Chlewicki, G., Greenberg, J. M., Patriarchi, P., & Perinotto, M. 1988, *A&AS*, 73, 195
- Andriesse, C. D., Piersma, T. R., & Witt, A. N. 1977, *A&A*, 54, 841
- Bazell, D. & Dwek, E. 1990, *ApJ*, 360, 142
- Burgh, E. B., McCandliss, S. R., Andersson, B-G, & Feldman, P. D. 2000, *ApJ*, 541, 250
- Burgh, E. B., McCandliss, S. R., Pelton, R., France, K., & Feldman, P. D. 2001, *Proc. SPIE*, 4498
- Buss, R. H., Allen, M., McCandliss, S., Kruk, J., Liu, J., & Brown, T. 1994, *ApJ*, 430, 630
- Calzetti, D., Bohlin, R. C., Gordon, K. D., Witt, A. N. & Bianchi, L. 1995, *ApJ*, 446, L97
- Cashwell, E. D. & Everett, C. J. 1959, *A Practical Manual on the Monte Carlo Method for Random Walk Problems* (New York: Pergamon Press)
- Cardelli, J. A., Clayton, G. C., & Mathis, J. S. 1989, *ApJ*, 345, 245
- Crawford, D. L., Barnes, J. V., & Golson, J. C. 1971, *AJ*, 76, 1058
- de Boer, K. S. 1983, *A&A* 125, 258
- DePoy, D. L., Lada, E. A., Gatley, I., & Probst, R. 1990, *ApJ*, 356, L55
- Field, D., Lemaire, J. L., Pineau Des Forets, G., Gerin, M., Leach, S., Rostas, F., & Rouan, D. 1998, *A&A*, 333, 280
- Fitzpatrick, E. L., & Massa, D. 1990, *ApJS*, 72, 163

- Flannery, B. P., Roberge, W., & Rybicki, G. B. 1980, *ApJ*, 236, 598
- Fogel, M. E. & Leung, C. M. 1998, *ApJ*, 501, 175
- Gatley, I., Hasegawa, T., Suzuki, H., Garden, R., Brand, P., Lightfoot, J., Glencross, W., Okuda, H., & Nagata, T. 1987, *ApJ*, 318, L73
- Gordon, K. D., K. A. Misselt, A. N. Witt, and G. C. Clayton, *ApJ*, 551, 269
- Gordon, K. D., Witt, A. N., Carruthers, G. R., Christensen, S. A., & Dohne, B. C. 1994, *ApJ*, 432, 641
- Hartig, G. F., Fastie W. G., and Davidsen, A. F. 1980, *Appl. Opt.*, 19, 729
- Hardie, R. H., Heiser, A. M., & Tolbert, C. R. 1964, *ApJ*, 140, 1472
- Harvey, P. M., Thronson, H. A., & Gatley, I. 1980, *ApJ*, 235, 894
- Heney, L. C. & Greenstein, J. L. 1941, *ApJ*, 93, 70
- Howe, J. E., Jaffe, D. T., Genzel, R., & Stacey, G. J. 1991, *ApJ*, 373, 158
- Hurwitz, M., Bowyer, S., & Martin, C. 1991, *ApJ*, 372, 167
- Jaffe, D. T., Zhou, S., Howe, J. E., Herrmann, F., Madden, S. C., Poglitsch, A., van der Werf, P. P., & Stacey, G. J. 1994, *ApJ*, 436, 203
- Jenniskens, P., Ehrenfreund, P., & Désert, F.-X. 1992, *A&A*, 265, L1
- Joseph, C. L., Snow, T. P., & Seab, C. G. 1989, *ApJ*, 340, 314
- Keski-Kuha, R. A. M., Osantowski, J. F., Herzig, H., Gum, J. S., & Toft, A. R. 1988, *Appl. Opt.*, 27, 2815
- Knapp, G. R., Brown, R. L., & Kuiper, T. B. H. 1975, *ApJ*, 196, 167
- Koornneef, J. 1983, *A&A*, 128, 84
- Kopp, M., Roueff, E., & Pineau des Forêts, G. 2000, *MNRAS*, 315, 37.
- Landini, M., Natta, A., Salinari, P., Oliva, E., & Moorwood, A. F. M. 1984, *A&A*, 134, 284
- Lee, T. A. 1968, *ApJ*, 152, 913
- Li, A. & Draine, B. T. 2001, *ApJ*, 550, L213
- Martin, P. G. & Whittet, D. C. B. 1990, *ApJ*, 357, 113
- Martini, P., Sellgren, K., & DePoy, D. L. 1999, *ApJ*, 526, 772
- Mathis, J. S. & Whiffen, G. 1989, *ApJ*, 341, 808
- McCandliss, S. R., Martinez, M. E., Feldman, P. D., Pelton, R., Keski-Kuha, R. A., & Gum, J. S. 1994, *Proc. SPIE*, 2011, 310
- McCandliss, S. R., Burgh, E. B., & Feldman, P. D. 2000, *Proc. SPIE*, 4139, 70
- McCartney, M. S. K., Brand, P. W. J. L., Burton, M. G., & Chrysostomou, A. 1999, *MNRAS*, 307, 315
- Meyer, D. M., Lauroesch, J. T., Sofia, U. J., Draine, B. T., & Bertoldi, F. 2001, *ApJ*, 553, L59
- Mookerjee, B., Ghosh, S. K., Rengarajan, T. N., Tandon, S. N., & Verma, R. P. 2000, *AJ*, 120, 1954
- Murthy, J., Dring, A., Henry, R. C., Kruk, J. W., Blair, W. P., Kimble, R. A., & Durrance, S. T. 1993, *ApJ*, 408, L97
- Racine, R. 1968, *AJ*, 73, 233
- Rieke, G. H. & Lebofsky, M. J. 1985, *ApJ*, 288, 618
- Roark, T., Roark, B., & Collins, G. W. 1974, *ApJ*, 190, 67
- Roberge, W. G., Dalgarno, A., & Flannery, B. P. 1981, *ApJ*, 243, 817
- Savage, B. D. & Mathis, J. S. 1979, *ARA&A*, 17, 73
- Schimminovich, D., Friedman, P. G., Martin, C., & Morrissey, P. F. 2001, *ApJ*, 563, L161
- Sellgren, K., Werner, M. W., & Dinerstein, H. L. 1992, *ApJ*, 400, 238

- Siegmund, O. H., Gummin, M. A., Stock, J. M., Marsh, D. R., Raffanti, R., & Hull, J. 1993, Proc. SPIE, 2006, 176
- Takami, M., Usuda, T., Sugai, H., Kawabata, H., Suto, H., & Tanaka, M. 2000, ApJ, 529, 268
- van Dishoeck, E. F. & Black, J. H. 1989, ApJ, 340, 273
- Weingartner, J. C. & Draine, B. T. 2001, ApJ, 548, 296
- Whittet, D. C. B. 1988, The observed properties of interstellar dust in the infrared. In *Dust in the Universe*, pp. 25–53.
- Whittet, D. C. B. & van Breda, I. G. 1978, A&A, 66, 57
- Witt, A. N. 1977, ApJS, 35, 21
- Witt, A. N. 1985, ApJ, 294, 216
- Witt, A. N., Friedmann, B. C., & Sasseen, T. P. 1997, ApJ, 481, 809
- Witt, A. N. & Gordon, K. D. 1996, ApJ, 463, 681
- Witt, A. N., Stecher, T. P., Boroson, T. A., & Bohlin, R. C. 1989, ApJ, 336, L21.
- Witt, A. N., Petersohn, J. K., Bohlin, R. C., O’Connell, R. W., Roberts, M. S., Smith, A. M., & Stecher, T. P. 1992, ApJ, 395, L5
- Witt, A. N., Petersohn, J. K., Holberg, J. B., Murthy, J., Dring, A., & Henry, R. C. 1993, ApJ, 410, 714
- Witt, A. N., Schild, R. E., & Kraiman, J. B. 1984, ApJ, 281, 708
- Witt, A. N., Walker, G. A. H., Bohlin, R. C., & Stecher, T. P. 1982, ApJ, 261, 492
- Wood, K. & Reynolds, R. J. 1999, ApJ, 525, 799
- Wyrowski, F., Walmsley, C. M., Goss, W. M., & Tielens, A. G. G. M. 2000, ApJ, 543, 245
- Yusef-Zadeh, F., Morris, M., & White, R. L. 1984, ApJ, 278, 186

TABLE 1
NEAR-INFRARED PHOTOMETRY OF
HD 37903.

Band	λ (μm)	Magnitude		
		Ref 1	Ref 2	Ref 3
I	0.88	7.52		
J	1.25	7.48	7.36	7.44
H	1.65		7.28	7.35
K	2.20	7.41	7.28	7.32
L	3.50	7.00	7.44	7.36
M	4.80			7.20

REFERENCES.—Ref 1 – Lee (1968); Ref 2 – Whittet & van Breda (1978); Ref 3 – DePoy et al. (1990)

TABLE 2
BEST FIT a AND g FROM RADIAL PROFILE FITTING.

Bandpass		Max. [†]	τ^{\ddagger}	Best-fit dust parameters	
λ_{min} (\AA)	λ_{max} (\AA)	radius ($''$)		a	g
990	1380	60	2.8	0.26	0.89
990	1380	60 N	2.8	0.27	0.87
990	1380	40 S	2.8	0.23	0.92
1050	1115	33	3.6	$0.23^{+0.20}_{-0.05}$	$0.88^{+0.07}_{-0.20}$
1115	1150	33	3.2	$0.21^{+0.25}_{-0.05}$	$0.89^{+0.07}_{-0.20}$
1150	1190	35	3.0	$0.22^{+0.25}_{-0.03}$	$0.90^{+0.04}_{-0.23}$
1240	1295	40	2.7	$0.31^{+0.12}_{-0.05}$	$0.85^{+0.05}_{-0.10}$
1310	1345	40	2.5	$0.35^{+0.15}_{-0.10}$	$0.83^{+0.10}_{-0.15}$
1345	1380	35	2.4	$0.39^{+0.12}_{-0.05}$	$0.80^{+0.05}_{-0.10}$

[†]Maximum radius of the fitting region

[‡]Intensity weighted optical depth for the given bandpass

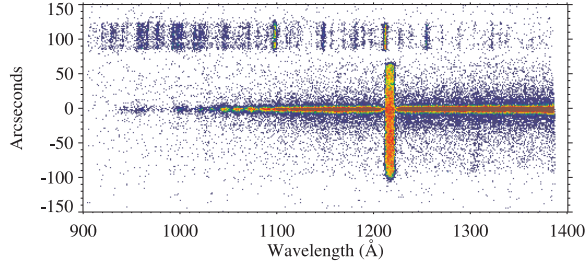


Fig. 1.— Long-slit spectral image of NGC 2023. The long axis of the slit was oriented with north at the top and south at the bottom. The spectrum at the top is that of the onboard calibration lamp. Red indicates the highest count rate regions.

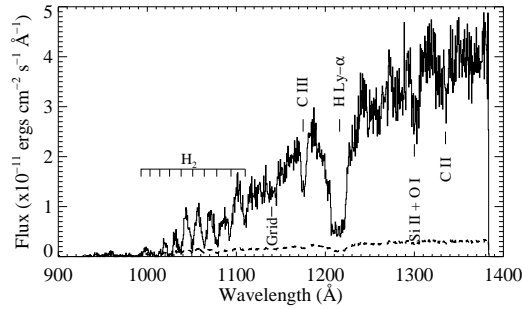


Fig. 2.— Flux calibrated spectrum of HD 37903. The error in the flux is shown as the dashed line. Strong stellar and interstellar absorptions are identified. The feature marked “grid” is an instrumental artifact.

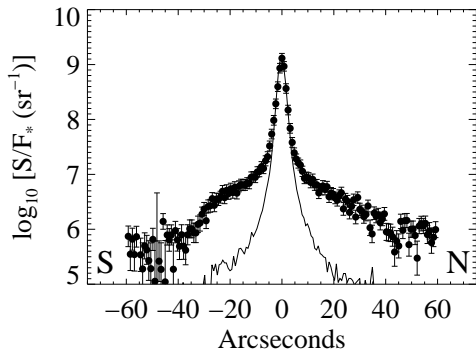


Fig. 3.— Spatial profile of nebular scattered light. Filled circles with error bars are the data, the solid line is the instrumental line spread function (LSF). The profile is centered on HD 37903 with positive offsets to the north.

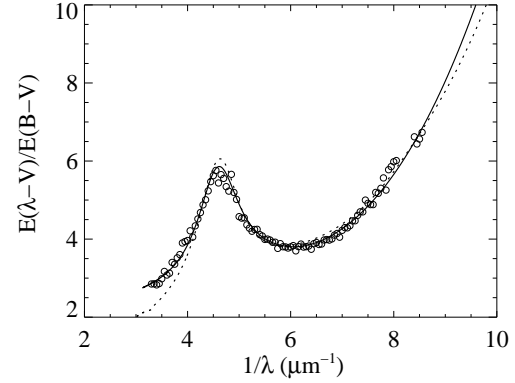


Fig. 4.— Derived extinction curve for HD 37903 from *IUE* data. The solid line is a fit following the parameterization of Fitzpatrick & Massa (1990). The dashed line is the extinction curve following the formula of Cardelli, Clayton, & Mathis (1989) for $R_V = 3.83$.

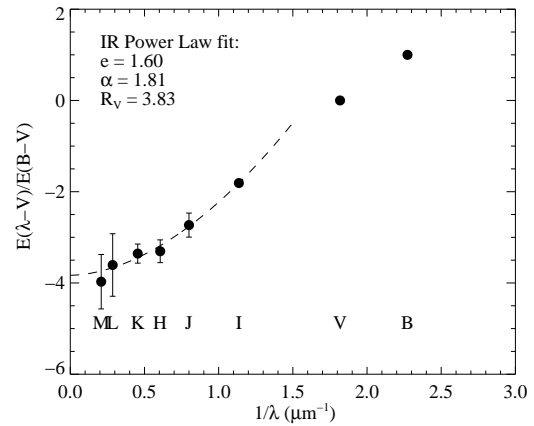


Fig. 5.— Infrared color excesses with extinction fit overplotted. Shown are the best fit parameters following the offset power law of Martin and Whittet (1990).

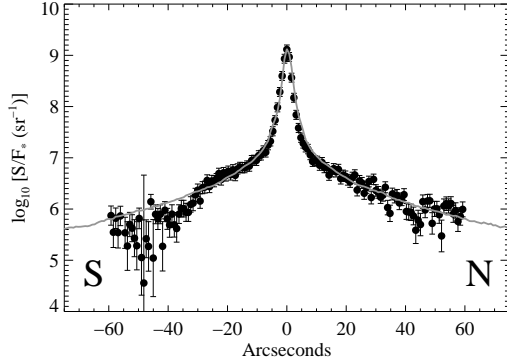


Fig. 6.— Slit profile of nebular surface brightness to stellar flux ratio for the “on-star” position. These data encompass the entire detector bandpass, excluding Ly- α . Overplotted is the model corresponding to the best fit a and g . The profile is centered on HD 37903 with positive offsets to the north.

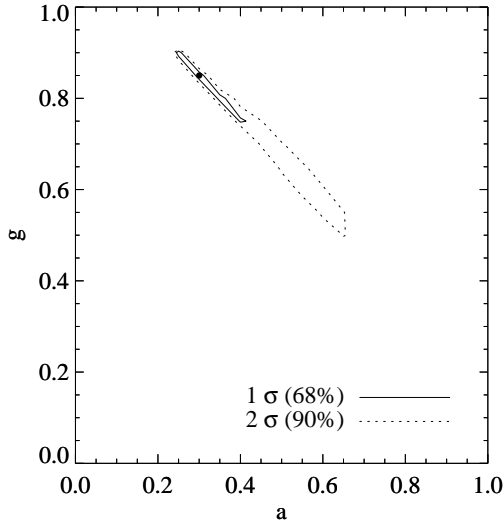


Fig. 7.— Confidence intervals from the χ^2 contours for the model fit of the nebular brightness radial profile for the 1240–1295 Å bandpass. The black dot indicates the best fit parameter values, corresponding to the minimum χ^2 . There is a degeneracy between the two parameters and the confidence tends toward lower g and higher a . The confidence intervals for the other bandpass fits are essentially of similar shape.

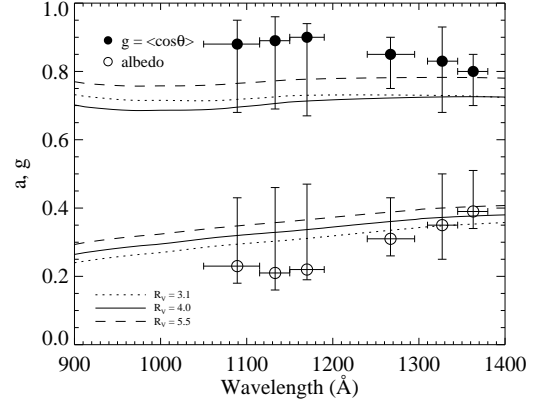


Fig. 8.— Derived values of a and g for the profile fits listed in Table 2. Theoretical predictions for various values of R_V from Weingartner & Draine (2001) are overplotted.

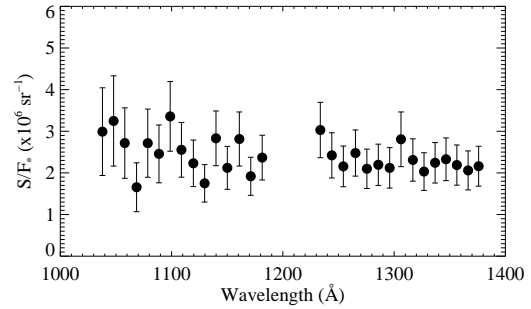


Fig. 9.— Spectrally binned S/F_* . The region around Ly- α is excluded.

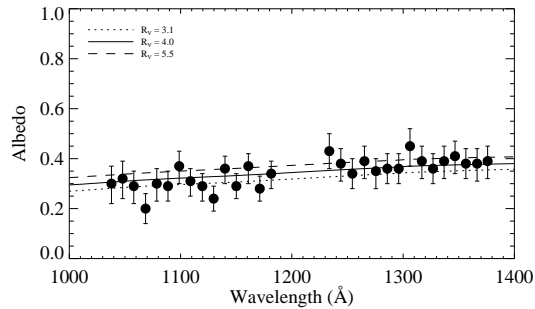


Fig. 10.— Derived wavelength dependence of albedo from model fitting of the spectrally binned data. The prediction for R_V values of 3.1, 4.0, and 5.5 from Weingartner & Draine (2001) are overplotted.

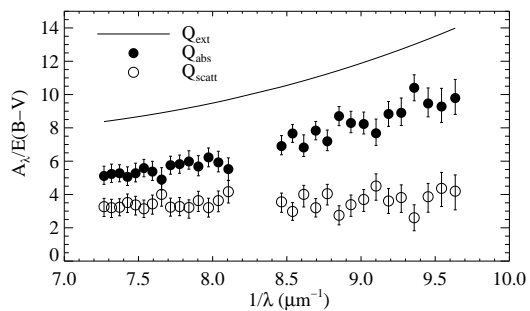


Fig. 11.— Relative values of the extinction, absorption, and scattering efficiencies derived from the best fit albedos. The dust extinction efficiency, Q_{ext} , is proportional to the extinction curve for HD 37903.